Sintering of porous strontium doped lanthanum manganite-yttria stabilized zirconia composite in controlled oxygen atmosphere at 1400 °C

Na Li, Manoj K. Mahapatra, Prabhakar Singh[*]

Center for Clean Energy Engineering, Department of Chemical, Materials and Biomolecular Engineering, University of Connecticut, Storrs, CT 06269, USA

HIGHLIGHTS

► Bulk density of porous LSM–YSZ composites increases with decrease in PO_2 during sintering.
► Formation of $La_2Zr_2O_7$ phase in LSM–YSZ composite is accelerated in lower sintering PO_2.
► Presence of 10–25% $La_2Zr_2O_7$ decreases LSM–YSZ thermal expansion coefficient by $\sim 1.2 \times 10^{-6}$ $^{\circ}C^{-1}$.

ARTICLE INFO

ABSTRACT

Role of oxygen partial pressure (PO_2) on the chemical and structural stability of porous strontium doped (20 mol%) lanthanum manganite (LSM)-8 mol% yttria stabilized zirconia (YSZ) composite has been studied. LSM and YSZ powders and pore former were mixed uniformly and uniaxially pressed into pellets. The pellets were sintered at 1400 °C for 2–10 h in 0.21–10^{-6} atm PO_2. Structural, chemical, and microstructural changes were examined using X-ray diffraction (XRD), scanning electron microscopy (SEM) and transmission electron microscopy (TEM) techniques. Density of the LSM–YSZ composites increased from 65% to 85% during sintering with decrease in the oxygen partial pressure. The crystal structures of LSM and YSZ maintained rhombohedral and cubic structure, respectively, under all sintering conditions. Formation of lanthanum zirconate ($La_2Zr_2O_7$) phase was observed in air after 10 h sintering and in 10^{-3} and 10^{-6} atm PO_2 after 2 h sintering. MnO_x was found in 10^{-6} atm PO_2 sintered composites. Lower PO_2 exposure also enhanced the grain growth. Thermal expansion coefficient (TEC) of the LSM–YSZ composites, determined by dilatometry, decreased from 11.5×10^{-6} $^{\circ}C^{-1}$ for the air sintered samples to 10.3×10^{-6} $^{\circ}C^{-1}$ for the samples sintered in 10^{-6} atm PO_2 due to the formation of $La_2Zr_2O_7$ phase.

Published by Elsevier B.V.

1. Introduction

Solid state electrochemical systems such as solid oxide fuel cells (SOFCs), solid oxide electrolysis cells (SOECs), and oxygen transport membrane (OTM) are attractive for power generation, carbon capture, hydrogen and syngas production and oxygen separation. YSZ and LSM have been extensively studied as electrolyte and electrode materials respectively [1–4] for SOFCs operating in 800–1000 °C temperature range. During the fabrication and operation of these systems, significant degradation in performance has been reported due to the formation of reaction products such as $La_2Zr_2O_7$ and $SrZrO_3$ at the LSM–YSZ interface [5].

The LSM–YSZ reactions have been extensively studied during the past two decades [6–10]. Formation of electrically insulating phases ($La_2Zr_2O_7$ and $SrZrO_3$) at the LSM–YSZ interface has been reported [11]. The electrical conductivity of the above phases is significantly lower than those of LSM and YSZ [12]. For example, at 1000 °C, the electrical conductivities of $La_2Zr_2O_7$, $SrZrO_3$ and $La_{0.8}Sr_{0.2}MnO_3$ are $\sim 2 \times 10^{-5}$ S cm^{-1}, 1×10^{-4} S cm^{-1}, and ~ 200 S cm^{-1}, respectively. The ionic conductivity of YSZ is 0.1 S cm^{-1} [11,13–15]. Formation of the zirconate phases changes the morphology of LSM and LSM–YSZ interface, decreases the length of triple phase boundary (electrochemically active area), and increases the interfacial resistance at the LSM–YSZ interface resulting in SOFC performance degradation [16]. For instance, the length of the triple phase boundary decreases from ~ 0.7 μm^{-1} to ~ 0.4 μm^{-1} and the interfacial resistance increases from ~ 100 Ω cm^2 to ~ 250 Ω cm^2 while the $La_2Zr_2O_7$ thickness at the LSM–YSZ interface increases from ~ 50 nm to ~ 70 nm [17].

The reaction between LSM and YSZ depends on the composition of $La_{1-x}Sr_xMnO_3$, yttria concentration and crystal structure of YSZ,

---

* Corresponding author. Tel.: +1 8604868379; fax: +1 8604868378.
E-mail address: singh@engr.uconn.edu (P. Singh).

the ratio between LSM and YSZ, characteristics of starting powder, sintering temperature, time, and atmosphere [18–26]. Several studies have indicated that $La_2Zr_2O_7$ forms for $x \geq 0.0$ and $SrZrO_3$ along with the $La_2Zr_2O_7$ starts to form for $x \geq 0.3$ [6,24,26], while other studies reported that both zirconates can form at $x \geq 0.17$, which is also consistent with thermodynamic calculations [19,23]. Formation of $SrZrO_3$ at 1:1 LSM and YSZ ratio and $La_2Zr_2O_7$ at 1:3 ratio was reported during annealing at 1000 °C in N_2 ($PO_2 \sim 10^{-5}$ atm) atmosphere [27]. However, $SrZrO_3$ formation was not observed when LSM and YSZ ratio ≥ 1.0 [19]. Although it has been reported widely in literature that the formation of zirconate phases depends on the starting powder characteristics, reaction temperature and exposure atmosphere, the effect remains little understood in terms of densification, grain growth and phase evolution [20]. The zirconate phases formation has been reported in a wide temperature range between 1000 °C and 1400 °C [24,26–28]. $SrZrO_3$ forms at higher temperature than that of $La_2Zr_2O_7$. For instance, $La_2Zr_2O_7$ forms at 1200 °C but $SrZrO_3$ forms at 1350 °C for $La_{0.6}Sr_{0.4}MnO_3$–YSZ composites sintered in air for 120 h [24]. The amount of the zirconate phases increases with increase in sintering time [24,25,27]. Interdiffusion of respective cations across the LSM–YSZ boundary during the sintering of LSM–YSZ has been reported to be responsible for zirconate phases formation [6,9,17,24,25,29]. Among all the elements in the LSM–YSZ composites, the diffusivity of manganese remains the highest [17], however, diffusion of manganese into the YSZ has not been observed by several researchers [23,30]. The contradictory nature of the above results related to LSM–YSZ interactions may be attributed to the difference in powder characteristics such as composition, morphology, surface area etc.

Most of the above reported studies have been conducted in air and electrochemical device operation conditions typically in the temperature range of 800–1100 °C. The understanding of the LSM–YSZ composite interaction under the device fabrication conditions remains largely unknown. Typical fabrication conditions include sintering at elevated temperatures in the range of 1200–1500 °C in air [31–34]. Role of sintering atmosphere on the air electrode densification, microstructural evolution and chemical interactions also remains unknown at these elevated temperatures. Above understanding is also considered useful for establishing degradation processes during cell operation at lower temperatures and oxygen pressures where oxygen partial pressure (PO_2) at the LSM–YSZ interface can be as low as 10^{-5} atm [5]. PO_2 change at the LSM–YSZ interface can occur during SOFC operation due to several reasons including intermixing of fuel gas and air due to internal cracks and seal leakage, changes in the component microstructure, and polarization of the electrodes [35].

It has been demonstrated that the lower PO_2 favors the formation of the zirconate phases [18,19,36]. These studies have not shown the detailed and systematic morphological evolution of reaction products and structure at lower PO_2. Recently, we have reported the role of PO_2 on the structural and morphological stabilities of LSM–YSZ composites, however, densification was not emphasized [37]. It was reported that porous electrodes accelerated the LSM–YSZ interaction when compared to dense electrodes [29]. Only $SrZrO_3$ formed for dense electrode, while both $La_2Zr_2O_7$ and $SrZrO_3$ formed for porous composite structure [28]. Even though porous cathodes are required for electrochemical systems applications, most of the studies have been conducted on dense LSM–YSZ composites [18,22,24,26]. In addition, the effect of zirconate phase on the thermal expansion coefficient (TEC) of the composite cathode remains unknown. The present study is focused on understanding the sintering and interaction behavior of LSM–YSZ composite structures under controlled oxygen partial pressure. A sintering temperature of 1400 °C was selected to represent the device sintering condition. An oxygen partial pressure range of $0.21–10^{-6}$ atm was selected to study the phase interaction and microstructural evolution.

2. Experimental

$La_{0.8}Sr_{0.2}MnO_3$ (particle size 0.5–1.8 μm, Inframat advanced materials, Connecticut), YSZ (particle size 0.3–1.4 μm, Fuel cell materials, Ohio), starch powders (particle size 30–45 μm) were mixed in 1:1:0.33 weight ratio. The mixed powders were uniaxially pressed into pellets at 100 MPa. The pressed pellets were bisque fired in air at 1000 °C for 2 h to burn the pore formers. The bisque fired samples were subsequently sintered at 1400 °C in a range of PO_2 (0.21–10^{-6} atm). The sintering atmosphere was achieved by using certified gas mixtures consisting of oxygen and nitrogen (Airgas east, Connecticut). The samples were sintered for 2, 5, and 10 h under a flowing gas atmosphere (flow rate of 40 sccm).

The density of the LSM-YSZ samples was measured by Archimedes method according to ASTM C20-97 standard. Phase characterization was performed by X-ray diffraction analysis using Cu Kα radiation (Bruker D8 advance X-Ray diffractometer). The semi-quantitative analysis to determine the amount of $La_2Zr_2O_7$ phase was performed by using the ratio of the 100% intensity reflection of $La_2Zr_2O_7$ and YSZ, taking plane multiplicity factors M_{hkl} into account [22,38].

The polished cross section was prepared using standard metallographic techniques and analyzed using scanning electron microscope (SEM, Quanta 600 FEI Company, Hillsboro, OR). The Energy dispersive spectroscopy module (EDS) attached to the SEM was used for elemental analysis.

The TEM specimens were prepared using a focused ion beam (FIB) instrument (FEI strata 400S, FEI company, Hillsboro, OR, 30 keV Ga+ ions) with a dual-beam column, combining a scanning electron beam and an ion beam in one unit. An Omniprobe nano-manipulator (Omniprobe auto probe ^{TM} 200) was used for the in situ TEM specimen lift-out technique. For the current study, a sample thickness between 75 and 100 nm was provided for TEM studies. TEM high resolution images, selected area diffraction pattern and TEM–EDS spot analysis were performed using JEOL 2010 FasTEM.

Thermal expansion properties were measured using the Netzsch 402PC dilatometer in air from room temperature to 1000 °C with a heating rate 5 °C min^{-1}. The sintered LSM–YSZ composite samples were cut to rectangular shape (10 × 2 × 3 mm) and used to measure TEC. Standard alumina rod was used for calibration. The dense YSZ and LSM samples sintered at 1400 °C for 10 h in air were used as reference for comparison.

3. Results

Observations related to sintered densities, compound formation, microstructure, elemental distribution, and thermal expansion are presented.

3.1. Density

Depending on the sintering atmospheres and exposure time, the average densities of the LSM–YSZ composites are in the range of 65–85% of theoretical density as shown in Fig. 1. The density of the LSM–YSZ composites increases from ~75% to ~80% while oxygen pressure in the sintering atmosphere decreases from 0.21 to 10^{-6} atm PO_2 for sintering time of 10 h. The density of the LSM–YSZ composites also increases from ~67% to ~75% with increasing sintering time from 2 h to 10 h for the samples sintered in air. Similar trend is observed for the samples sintered in lower PO_2. It
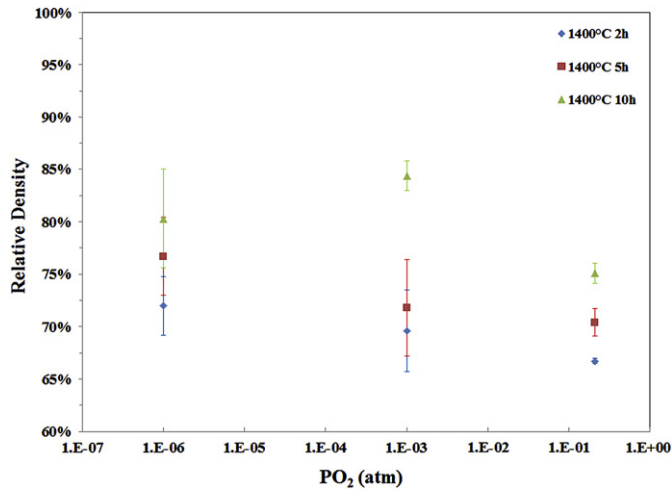
Fig. 1. Relative density of LSM−YSZ composites sintered at 1400 °C in different atmospheres for 2 h, 5 h and 10 h.
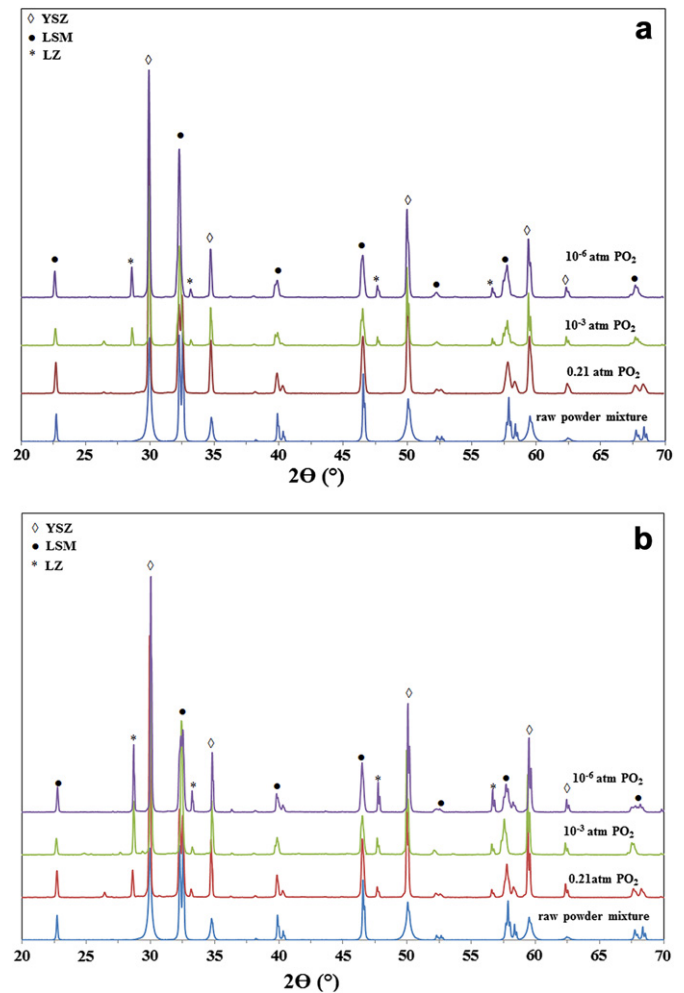

Fig. 2. XRD patterns of the LSM−YSZ composites in different sintering atmospheres (a) samples sintered at 1400 °C for 2 h in 10^{-6} atm, 10^{-3} atm and air (b) samples sintered at 1400 °C for 10 h in 10^{-6} atm, 10^{-3} atm and air.

can be noted that the density value of the LSM−YSZ sample is scattered within ±5% and the deviation from the average value increases with lowering PO_2 (Fig. 1). It is also observed that the density of the composites sintered in 10^{-3} atm PO_2 for 10 h is higher (~85%) than the samples sintered in 10^{-6} atm PO_2 for the same time, however, within the standard deviation range. The large deviation from the average density values may be attributed to the localized pore distribution in the samples. The amount of porosity may also vary from sample to sample resulting in the change in the interaction volume of solids with the sintering atmospheres, leading to large variation in the density values. Nonetheless, it can be concluded that the density of the LSM−YSZ composites increases with decrease in PO_2 and increase in sintering time.

3.2. Phase evolution

The effect of sintering atmosphere and exposure time on the compound formation in the LSM−YSZ composites were analyzed by XRD (Fig. 2). Cubic zirconia (JCPDS number: 00-030-1468) and rhombohedral LSM (JCPDS number 00-053-0058) are observed for all the samples. The crystal structure of the LSM and YSZ does not change with sintering condition as observed from the identical peak positions with that of raw powders. New phase, cubic $La_2Zr_2O_7$ (JCPDS number: 01-070-5602), is found for the samples sintered in air for 10 h only, and in 10^{-3} and 10^{-6} atm PO_2 for all the sintering times.

The amount of $La_2Zr_2O_7$ was determined by the intensity ratio of X-ray diffraction line of the (222) plane of $La_2Zr_2O_7$ to that of (111) plane of YSZ since the above lines are the 100% intensity peaks of $La_2Zr_2O_7$ and YSZ, respectively, and both peaks have same multiplicity factors ($M_{hkl} = 8$) [38]. Fig. 3 showed that the relative amount of $La_2Zr_2O_7$ increases with decreasing PO_2 of sintering atmosphere and increasing sintering time. These observations indicate that reduced sintering atmosphere and the prolonged sintering time favor the formation of $La_2Zr_2O_7$.

3.3. Microstructure

Microstructural features of sintered LSM−YSZ composites are shown in Fig. 4. Fig. 4(a) shows the cross section of sample sintered at 1400 °C in air for 2 h. Two main phases are homogeneously distributed into the samples. Color contrast and elemental analysis, performed by SEM−EDS technique, indicates the dark phase to be
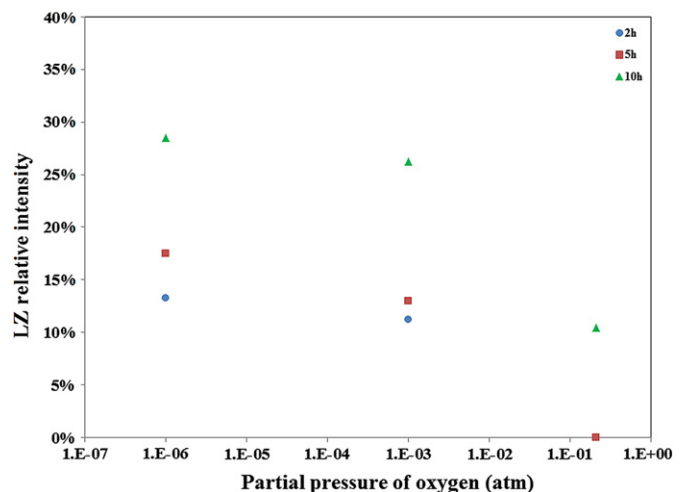
Fig. 3. $La_2Zr_2O_7$ (LZ)/YSZ relative amount with different atmosphere for 2 h, 5 h and 10 h.
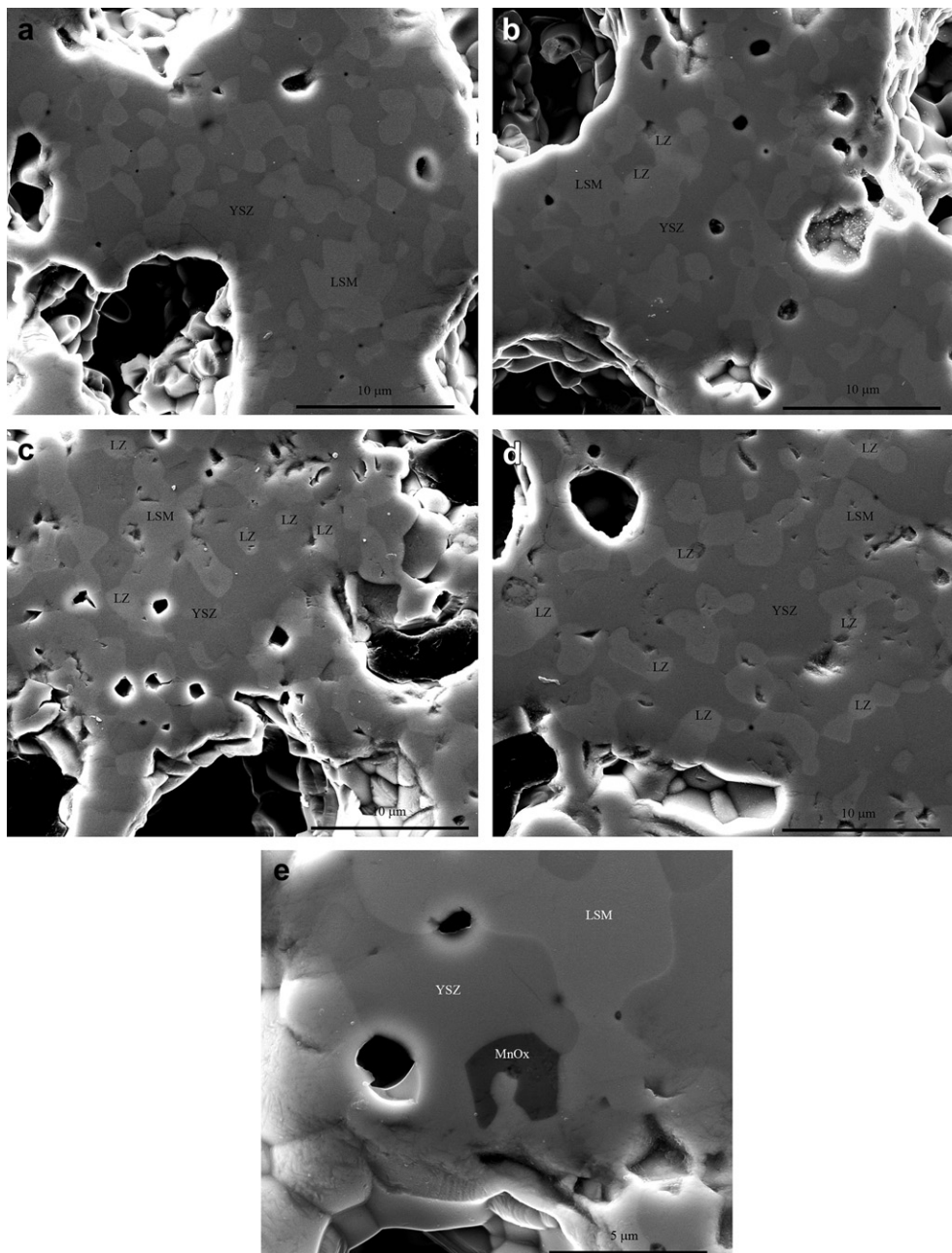
Fig. 4. SEM of the cross section of samples sintered at 1400 °C in (a) air for 2 h, (b) air for 10 h, (c) 10^{-3} atm PO_2 for 10 h, and (d) and (e) 10^{-6} atm PO_2 for 10 h.

YSZ, the bright phase to be LSM. 5 h sintered samples have the similar features. The SEM image is not shown here for brevity. With the sintering time increased to 10 h (Fig. 4(b)), presence of $La_2Zr_2O_7$ was identified as the brightest contrast, confirmed by EDS analysis under SEM observation.

All the samples sintered in 10^{-3} atm PO_2 shows three phases LSM, YSZ and $La_2Zr_2O_7$ (Fig. 4c). In addition to the mentioned three phases (Fig. 4d), few MnO_x grains about ~2 μm size are also found in the samples sintered in 10^{-6} atm PO_2 as shown in Fig. 4(e). The $La_2Zr_2O_7$ phase is found after 2 h sintering in these low PO_2 condition. The amount of the $La_2Zr_2O_7$ was found to increase with decrease in PO_2 and increase in sintering time. The grain sizes of all the phases vary in a wide size range for all the samples due to the variation in particle sizes of the starting LSM (0.5–1.8 μm) and YSZ (0.3–1.4 μm) powders. The grain size of both LSM and YSZ increases

with decrease in PO_2. For example, the average grain size of LSM and YSZ changed from ~1.6 to ~2.9 μm and ~1.8 to ~2.7 μm respectively, during sintering in air and 10^{-3} atm PO_2. During sintering in 10^{-6} atm PO_2, the grain size for LSM and YSZ further increased to ~3.3 and ~2.8 μm respectively. For $La_2Zr_2O_7$, the average grain size remained around 2.0 μm for 10 h sintering in all the sintering atmospheres.

The elemental composition of the observed phases was obtained by averaging the SEM–EDS spot (~20 spots) analysis results. For brevity, the elemental compositions of different phases obtained from EDS analysis are shown only for the samples sintered for 10 h as no significant difference in composition was found for the different sintering duration. For the air sintered sample, YSZ contains ~7 at% La and ~10 at% Mn, whereas LSM contains ~7 at% Zr. On changing the sintering atmosphere to 10^{-3} atm PO_2; YSZ

Fig. 5. TEM image of sample sintered at 1400 °C in 10^{-6} atm PO$_2$ for 10 h.

Fig. 6. Selected area diffraction pattern of La$_2$Zr$_2$O$_7$ (LZ) with the zone axis [011].

shows ~7 at% La, ~11 at% Mn, and LSM shows ~2 at% Zr. In 10^{-6} atm PO$_2$ sintering atmosphere, Mn content in the YSZ increased to ~14 at% while the contents of the other elements remained similar to those observed in the 10^{-3} atm PO$_2$ sintering atmosphere. The increased amount of Mn in YSZ and reduced amount of Zr in LSM in the samples sintered in 10^{-6} atm PO$_2$, when compared to those of the air sintered samples. This suggests that the elemental diffusion from LSM into YSZ becomes more pronounced with decreasing PO$_2$ as compared to the diffusion from YSZ into LSM.

For better understanding of the elemental distribution, a thin sample (150–200 nm) having all the three phases (LSM, YSZ and LZ) was prepared using focused ion beam (FIB) from the LSM–YSZ composite sintered in 10^{-6} atm PO$_2$. Fig. 5 shows a high-resolution bright field image. YSZ, LSM, and La$_2$Zr$_2$O$_7$ grains were observed and confirmed by TEM–EDS analysis (Table 1). The LZ grains were characterized by selected area electron diffraction (SAED). Fig. 6 shows the fcc pyrochlore structure of La$_2$Zr$_2$O$_7$ with the zone axis of [011]. The lattice image (Fig. 7) clearly shows the interface between La$_2$Zr$_2$O$_7$ and YSZ.

3.4. Thermal expansion behavior

The thermal expansion coefficients (TEC) of the porous LSM–YSZ composites are shown in Table 2. The TECs of dense YSZ and LSM are also shown for reference purposes. The TEC values of the LSM and YSZ are 12.3×10^{-6} °C^{-1} and 10.8×10^{-6} °C^{-1} respectively from room temperature to 1000 °C, consistent with literature [39–41]. The TEC of the LSM–YSZ composite sintered in air for 2 h at 1400 °C is 11.5×10^{-6} °C^{-1}, and is in agreement with the mixing rule of the composite. For the samples sintered in lower PO$_2$, the

TEC value decreased from 11.5 to 10.3×10^{-6} °C^{-1}. Lowering of the TEC is assigned to the presence of La$_2$Zr$_2$O$_7$ phase (11–28%) in the samples sintered in 10^{-3} and 10^{-6} atm PO$_2$. The TEC values of La$_2$Zr$_2$O$_7$ were reported in the range of 9.0–9.3×10^{-6} °C^{-1} [22,42,43].

4. Discussion

The PO$_2$ range used in the present work (0.21–10^{-6} atm) is well within the chemical and structural stability region for both LSM
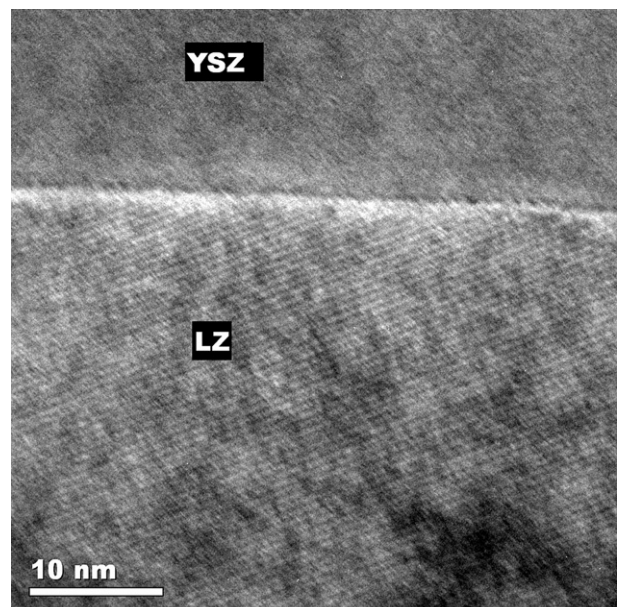
Table 1
TEM–EDS results for LSM–YSZ composite sintered at 1400 °C in 10^{-6} atm PO$_2$ for 10 h.

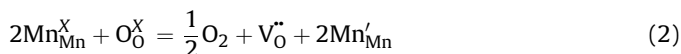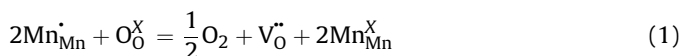| Preparation condition	La	Sr	Mn	Y	Zr	Compounds
10^{-6} atm PO$_2$	8.5	0	10.6	13.4	67.5	YSZ
1400 °C	52.0	8.4	36.1	0.7	2.8	LSM
10 h	56.4	0	0.5	4.1	39.0	LZ

Fig. 7. Lattice image of YSZ/La$_2$Zr$_2$O$_7$ (LZ) interface with the zone axis [011].

Table 2
Thermal expansion coefficient (from room temperature to 1000 °C) of samples.

Composition	TEC ($\times 10^{-6}$ °C^{-1}) this study	TEC ($\times 10^{-6}$ °C^{-1}) reference
YSZ	10.8	10.3 [36], 10.9 [37]
LSM	12.3	11.7 [37], 11.6 [38]
LZ		9 [22], 9.2 [39], 9.3 [40]
YSZ–LSM sintered in air for 2 h	11.5	
YSZ–LSM sintered in 10^{-3} atm PO$_2$ for 10 h	10.3	
YSZ–LSM sintered in 10^{-6} atm PO$_2$ for 10 h	10.3	

and YSZ [44]. The technical discussion is focused on observations related to (a) higher solubility of Mn in YSZ at lower PO$_2$ (b) enhanced densification with decrease PO$_2$ (c) increased formation of La$_2$Zr$_2$O$_7$ at lower PO$_2$ and (d) presence of MnO$_x$ at lower PO$_2$.

Mn solubility (8–14%) in YSZ has been reported during the sintering of LSM–YSZ. Mn ions diffuse readily in YSZ due to its smaller ionic radii and the highest diffusivity among the constituent lanthanum and strontium ions [6,27]. The Mn in solid solution is a mixture of Mn^{3+} and Mn^{2+} [45]. The diffusion of Mn from LSM into YSZ changes the oxygen stoichiometry as well as influences the (La + Sr) to Mn ratio in LSM [7,46]. At lower PO$_2$, manganese ions reduce to lower valence state according to Ref.[47]

$$2Mn_{Mn}^{\cdot} + O_O^X = \frac{1}{2}O_2 + V_O^{\cdot\cdot} + 2Mn_{Mn}^X \tag{1}$$

$$2Mn_{Mn}^X + O_O^X = \frac{1}{2}O_2 + V_O^{\cdot\cdot} + 2Mn_{Mn}' \tag{2}$$

where $V_O^{\cdot\cdot}$, $Mn_{Mn}^{\cdot}$, Mn_{Mn}^X, and Mn_{Mn}' are oxygen vacancy, Mn^{4+}, Mn^{3+}, and Mn^{2+}, respectively. Oxygen vacancies increase due to change in the oxidation state of manganese ions as stated above [48]. Substitution of Mn at the Zr site in YSZ also has the tendency to increase the oxygen ion vacancy according to reactions:

$$MnO_{ZrO_2} = Mn_{Zr}'' + V_O^{\cdot\cdot} + O_O^X \tag{3}$$

Where Mn_{Zr}'' is Mn^{2+} on Zr site in YSZ. It has been calculated that the MnO$_x$ solubility in c-ZrO$_2$, the amounts of Mn^{2+} and Mn^{3+}, vary with PO$_2$ [46]. In lower PO$_2$ region, mainly Mn^{2+} dissolves in ZrO$_2$ and its solubility is higher than Mn^{4+} and/or Mn^{3+} solubility in air [49]. As a result, the amount of manganese in ZrO$_2$ increases from 10 at% Mn to 14 at% while sintering atmosphere changes from air to 10^{-6} atm PO$_2$. Our experimental findings confirm and validate the theoretical evaluation [46].

The overall grain size of the LSM–YSZ composites sintered in 10^{-3} atm and 10^{-6} atm PO$_2$ is larger than those for the samples sintered in air. In reduced atmospheres, oxygen vacancies increase due to changes in the oxidation state of manganese ions as stated above (reactions (1) and (2)). The oxygen vacancies enhance the atomic mobility to the grain boundaries and free surfaces causing the development of larger grain size. For LSM, cation mobility has been reported to be rate-limiting for sintering [50,51]. The diffusion of oxygen in LSM creates a cation vacancy gradient [52] and diffusion increases with decreased oxygen partial pressure [53] that provides a greater driving force for sintering. Our observation on increase in densification is consistent with above explanation.

The formation of lanthanum zirconate phase is influenced by PO$_2$ and can be discussed from two aspects. Firstly, La$_2$O$_3$–MnO$_x$–ZrO$_2$ chemical potential diagram shows that lanthanum manganite and zirconia cannot coexist in equilibrium without La$_2$Zr$_2$O$_7$

formation at high temperatures ($\geq$1000 °C) [30]. The reaction can be written as

$$LaMnO_3 + ZrO_2 = \frac{1}{2}La_2Zr_2O_7 + MnO_x + \left(\frac{3}{4} - \frac{1}{2}x\right)O_2 \tag{4}$$
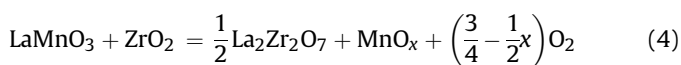
The forward reaction rate of the reaction (4) increases with decreasing PO$_2$ favoring lanthanum zirconate formation in lower PO$_2$. Secondly, the diffusivity of manganese is the highest among all the elements in LSM (La, Sr, and Mn), supported by the highest amount of Mn (10–14 at%) in YSZ followed by La (7–8 at%) and Sr (0–2 at%) from our EDS data. The Gibbs free energy value for formation of La$_2$Zr$_2$O$_7$ (-146.2×5.0 kJ mol^{-1} at 1200 K) is more negative than that of SrZrO$_3$ (-92.01 kJ mol^{-1} at 1200 K) [36,53]. Also, the activation energy for La$_2$Zr$_2$O$_7$ formation (17.5×1.8 kJ mol^{-1}) is lower than that of SrZrO$_3$ (18.8 ± 1.9 kJ mol^{-1}) [23]. As a result, La$_2$Zr$_2$O$_7$ but no SrZrO$_3$ is observed in this study.

Manganese oxide has been observed in the LSM–YSZ composites sintered in 10^{-6} atm PO$_2$. Formation of MnO$_x$ at lower oxygen pressure (10^{-6} atm) is explained on the basis of the feasibility of reaction (4) where lower oxygen pressure favors MnO$_x$ and La$_2$Zr$_2$O$_7$ formation. The absence of manganese oxide for the samples sintered at higher oxygen pressures is considered to be due to evaporation of the MnO$_x$ from the porous sample and its deposition at the sintering crucible wall. These observations are also supported by our previous study [37].

5. Conclusion

The densification and interaction of LSM–YSZ in porous composite structures has been examined as a function of oxygen partial pressure during sintering at 1400 °C. Our observations indicate enhanced densification and grain growth with reduction in oxygen partial pressure and are attributed to changes in the defect structure. Lowering of the oxygen partial pressure resulted in the formation of La$_2$Zr$_2$O$_7$ and MnO$_x$ in the composite. Thermal expansion coefficient of the composite also decreases with increase in the amount of the zirconate phase.

References

[1] B.C.H. Steele, J. Mater. Sci. 36 (2001) 1053–1068.
[2] J.H. Kuo, H.U. Anderson, J. Solid State Chem. 83 (1989) 52–60.
[3] M. Ni, M.K.H. Leung, D.Y.C. Leung, Int. J. Hydrogen Energy 33 (2008) 2337–2354.
[4] M. Dhallu, J.A. Kilner, J. Fuel Cell. Sci. Technol. 2 (2005) 29–33.
[5] Y.L. Liu, A. Hagen, R. Barfod, M. Chen, H.J. Wang, F.W. Poulsen, P.V. Hendriksen, Solid State Ionics 180 (2009) 1298–1304.
[6] K. Kleveland, M. Einarsrud, C.R. Schmidt, S. Shamsili, S. Faaland, K. Wiik, T. Grande, J. Am. Ceram. Soc. 82 (1999) 729–734.
[7] H. Yokokawa, T. Horita, N. Sakai, T. Kawada, M. Dokiya, in: Ulf Bossel (Ed.), First European Solid Oxide Fuel Cell Forum Proceedings, vol. 1, European Solid Oxide Fuel Cell Forum Publishers, Oberrohrdorf, Switzerland, 1994, pp. 425–434.
[8] Y. Takedal, Y. Sakaki, T. Ichikawa, N. Imanishi, O. Yamamoto, Solid State Ionics 72 (1994) 257–264.
[9] H. Taimatsu, K. Wada, H. Kaneko, H. Yamamura, J. Am. Ceram. Soc. 75 (1992) 401–405.
[10] M. Backhaus-Ricoult, Solid State Ionics 177 (2006) 2195–2200.
[11] S.P. Jiang, J. Mater. Sci. 43 (2008) 6799–6833.

[12] F.W. Poulsen, N.V. Puil, Solid State Ionics 53—56 (1992) 777—783.
[13] J.A. Labrincha, J.R. Frade, F.M.B. Marques, J. Mater. Sci. 28 (1993) 3809—3815.
[14] H.Y. Lee, S.M. Oh, Solid State Ionics 90 (1996) 133—140.
[15] C. Brugnoni, U. Ducati, M. Scagliotti, Solid State Ionics 76 (1995) 177—182.
[16] A. Hagen, Y.L. Liu, R. Barfod, P.V. Hendriksen, J. Electrochem. Soc. 155 (2008) B1047—B1052.
[17] A. Chen, J.R. Smith, K.L. Duncan, R.T. DeHoff, K.S. Jones, E.D. Wachsman, J. Electrochem. Soc. 157 (2010) B1624—B1628.
[18] M. Chen, Y.L. Liu, A. Hagen, P.V. Hendriksen, F.W. Poulsen, Fuel Cells 09 (2009) 833—840.
[19] C. Levy, Y. Zhong, C. Morel, S. Marlina, J. Electrochem. Soc. 157 (2010) B1597—B1601.
[20] H.S. Song, W.H. Kim, S.H. Hyun, J. Moon, J. Electroceram. 17 (2006) 759—764.
[21] C. Clausen, C. Bagger, J.B. Bilde-Sorensen, A. Horsewell, Solid State Ionics 70—71 (1994) 59—64.
[22] M. Mori, T. Abe, H. Itoh, O. Yamamoto, G.Q. Shen, Y. Takeda, N. Imanishi, Solid State Ionics 123 (1999) 113—119.
[23] J.A.M. van Roosmalen, E.H.P. Cordfunke, Solid State Ionics 52 (1992) 303—312.
[24] K. Wiik, C.R. Schmidt, S. Faaland, S. Shamsili, M. Einarsrud, T. Grande, J. Am. Ceram. Soc. 82 (1999) 721—728.
[25] C.C.T. Yang, W.C.J. Wei, A. Roosen, J. Am. Ceram. Soc. 87 (2004) 1110—1116.
[26] G. Stochniol, E. Syskakis, A. Naoumidis, J. Am. Ceram. Soc. 78 (1995) 929—932.
[27] A. Chen, G. Bourne, K. Siebein, R. DeHoff, E. Wachsman, K. Jones, J. Am. Ceram. Soc. 91 (2008) 2670—2675.
[28] M.C. Brant, T. Matencio, L. Dessemond, R.Z. Domingues, Solid State Ionics 177 (2006) 915—921.
[29] A. Grosjean, O. Sanseau, V. radmilovic, A. Thorel, Solid State Ionics 177 (2006) 1977—1980.
[30] A. Mitterdorfer, L.J. Gaukler, Solid State Ionics 111 (1998) 185—218.
[31] L.J.H. Kuo, P. Singh, R.J. Ruka, T.R. Vasilow, R.J. Bratton, US Patent, 056861982, 1997.
[32] P. Sarkar, H. Rho, US Patent, 7736772 B2, 2010.
[33] E. EI Batawi, P. Munoz, D. Nguyen, US Patent, 0043010 A1, 2012.
[34] M.F. Mahoney, Y. Narendar, H. Huang, WO Patent, 082326 A2, 2011.
[35] A.V. Virkar, J. Power Sources 172 (2007) 713—724.
[36] K.T. Jacob, Y. Wased, Metall. Mater. Trans. B 26 (1995) 775—781.
[37] M.K. Mahapatra, S. Bhowmick, N. Li, P. Singh, J. Eur. Ceram. Soc. 32 (2012) 2341—2349.
[38] S. Faaland, M.A. Einarsrud, K. Wiik, T. Grande, J. Mater. Sci. 34 (1999) 957—966.
[39] D. Lee, J.H. Han, Y. Chun, R.H. Song, D.R. Shin, J. Power Sources 166 (2007) 35—40.
[40] F. Tietz, Ionics 5 (1999) 129—139.
[41] G. Corbel, S. Mestiri, P. Lacorre, Solid State Sci. 7 (2005) 1216—1224.
[42] H. Zhou, D. Yi, Z. Yu, L. Xiao, J. Alloys Compd. 438 (2007) 217—221.
[43] Z. Xu, L. He, X. Zhong, J. Zhang, X. Chen, H. Ma, X. Cao, J. Alloys Compd. 480 (2009) 220—224.
[44] A.N. Grundy, B. Hallstedt, L.J. Gauckler, Calphad 28 (2004) 191—201.
[45] C.C. Appel, G.A. Botton, A. Horsewell, W.M. Stobbs, J. Am. Ceram. Soc. 82 (1999) 429—435.
[46] M. Chen, B. Hallstedt, L.J. Gauckler, Solid State Ionics 176 (2005) 1457—1464.
[47] Q.H. Wu, M. Liu, W. Jaegermann, Mater. Lett. 59 (2005) 1980—1983.
[48] L. Rørmark, K. Wiik, S. Stølen, T. Grande, J. Mater. Chem. 12 (2002) 1058—1067.
[49] J.W. Stevenson, P.F. Hallman, T.R. Armstrong, L.A. Chick, J. Am. Ceram. Soc. 78 (1995) 507—512.
[50] J.A.M. Van Roosmalen, E.H.P. Cordfunke, J.P.P. Huijsmans, Solid State Ionics 66 (1993) 285—293.
[51] R.A. De Souza, J.A. Kilner, J.F. Walker, Mater. Lett. 43 (2000) 43—52.
[52] B.P. McCarthy, L.R. Pederson, R.E. Williford, J. Am. Ceram. Soc. 92 (2009) 1672—1678.
[53] K.T. Jacob, N. Dasgupta, Y. Waseda, J. Am. Ceram. Soc. 81 (1998) 926—930.